Numerically-based method for fracture characterization of Mode I-dominated two-dimensional delamination in FRP laminates

Aida Cameselle-Molares[a], Anastasios P. Vassilopoulos[a], Jordi Renart[b,c], Albert Turon[b], Thomas Keller[a]

[a] Composite Construction Laboratory (CCLab), École Polytechnique Fédérale de Lausanne (EPFL), Station 16, Bâtiment BP, CH-1015 Lausanne, Switzerland

[b] AMADE, Mechanical Engineering and Industrial Construction Department, Universitat de Girona, Campus Montilivi s/n, Girona, Spain

[c] Serra Húnter Fellow, Generalitat de Catalunya, Spain

Abstract

A new numerically-based method suitable for determining the total strain energy release rate (SERR) involved in two-dimensional (2D) Mode I-dominated delamination under opening loads in FRP laminates is presented. The method is based on the mutual dependence of the load vs opening displacement curves slope exhibited after the full development of the fracture process zone (FPZ) and the total SERR involved in the delamination process. The equation relating these parameters is derived from three-dimensional finite element analyses performed using simple linear-softening cohesive zone models. Considering that the load-displacement curve reflects the overall fracture behavior, the above-mentioned slope correlates with the mean total SERR required to propagate the total 2D crack, independently of any local total SERR's variation along the crack front. Thus, the same mean cohesive zone model is used in all directions. By substituting the corresponding experimental slope of the load-displacement curves in the derived equation the total SERR is obtained. The method was validated using the experimental results from three types of GFRP/epoxy laminates with different fiber architectures. The measurement of the crack front is not required and the method is valid for any fiber architecture, crack shape and boundary conditions in Mode I-dominated and opening loading cases.

Keywords: 2D crack propagation; SERR; fracture; delamination; finite element analysis.

1. Introduction

Traditionally, most delamination or debonding investigations of fiber-reinforced polymer (FRP) materials have been limited to beam-like specimens such as double cantilever beams (DCBs) for opening fracture modes (Mode I) or end-loaded split (ELS) and mixed-mode bending (MMB) for shear modes (Mode II and mixed-Mode I/II respectively) [1-4]. The fracture values obtained from these standard fracture mechanics experiments were often employed in the prediction of the damage response in more complex structural components [5, 6]. Nevertheless, some conditions inherent to the standard beam-like specimens, e.g. constant crack width or unique direction of crack propagation (1D), do not correspond to real delamination scenarios, where cracks propagate in the delamination plane (2D) without any space or shape restrictions. Thus, fracture properties derived from 1D experiments may not be applicable for the prediction of the fracture behavior of actual structural components.

A more realistic description of the 2D fracture behavior was suggested by the authors by performing experimental [7] and numerical [8] investigations of 2D delamination in laminated GFRP plates with embedded cracks growing under opening loads. The transparency of the laminates enabled the crack front to be monitored during the fracture process. In [8], a significant increase in the total SERR (i.e. the SERR achieved after the full development of the fiber-bridging) involved in the 2D delamination, when compared to the total SERR value derived from standard (1D) fracture experiments, was reported. This increase was caused by an increase in the amount of fiber-bridging developed as a result of two factors: 1) the increment in the flexural stiffness (from beam to plate), and 2) stress stiffening due to the in-plane stretching of the delaminated regions of the plates (as a result of the boundary conditions inherent to an embedded crack), which both reduced the rotation of the crack faces. In 1D delamination cases where non-negligible fracture process zones (FPZs) with significant fiber-bridging developed, a flexural stiffness dependency of the total SERR was already observed [9-16].

The compliance results obtained in [7] for the 2D laminated plates were affected not only by the propagation of the crack but also by the additional stress stiffening due to the stretching of the cracked region. Thus, existing compliance-based data reduction methods used to derive the total SERR in beam-like specimens [2-4, 17], where the required compliance values after crack initiation only reflect the propagation of the crack, are no longer applicable in 2D delamination cases. Furthermore, the required monitoring of the 2D crack front, i.e. the crack length in the

different directions, is not simple in cases of opaque laminates. The contour integral method (*J*-integral) [11, 14, 18, 19], which can provide closed formulations that do not depend on the compliance or the crack length, generally requires measuring the rotations of the specimens however, which leads to complex experimental set-ups in 2D delamination cases.

In order to estimate the total SERR involved in 2D delamination, numerical simulations using cohesive elements to model the crack interface were carried out in [8]. A complex traction-separation law combining linear and exponential softening was implemented in the numerical model to define the cohesive behavior. The different cohesive parameters of the law were iteratively adjusted to simulate the experimental load-displacement and crack-displacement curves, thus involving considerable time and computational cost. The measurement of the 2D crack front, visually accessible thanks to the translucency of the GFRP plates, was therefore essential in this process.

To overcome these difficulties, a novel and simpler numerically-based method, suitable for determining the total SERR involved in Mode I-dominated 2D in-plane delamination of FRP laminated plates with internal embedded defects and subjected to opening loads, is presented, applied and validated in this work. The method is based on two particular findings reported in the former work [8], i.e. 1) the existing dependence between the slope of the load-displacement curve exhibited after the full development of the FPZ and the value of the total SERR, and 2) the independence of the latter from the selected shape of the traction-separation laws. As a result, cohesive elements with simple traction-separation laws are used and only the slope of the linear part of the experimental load-displacement results is required to apply the method. Since no monitoring of the crack front is necessary either, this implies a considerable simplification of both the experimental and numerical demands. The backbone of the method is based on an inverse analysis [20-25] where, through the fitting of the above-defined experimental slope, the total SERR is obtained. However the method builds up on the above-mentioned novel findings and their combination and allows the estimation of the total SERR in 2D crack propagation under Mode I and opening in an affordable way, i.e. without excessive experimental and numerical efforts.

The relevant previous experimental [7] and numerical [8] results, necessary for understanding the new method, are summarized in Sections 2 and 3 respectively. Section 2 is complemented

with an extended discussion of the experimental results, not included in the previous work. The new method is described in Section 4 and validated in Section 5.

2. Experimental investigation of laminated plates: results and discussion

2.1. Previous results and discussion

An experimental investigation of the 2D delamination behavior of GFRP/epoxy laminated plates under quasi-static out-of-plane opening loading was presented in [7]. A circular embedded pre-crack was introduced in the center and midplane of the plates. The experimental set-up, similar for all the laminates, is presented in Fig. 1. A total of six pairs of plates, using six different types of glass reinforcements, were investigated. The investigation presented here involves the continuous filament mat reinforcement (plates CFM.1/2) and two types of woven fabrics with different proportions of reinforcement in the warp/weft directions, i.e. 50/50 (plates W50.50.1/2) and 60/40 (plates W60.40.1/2). The properties of the epoxy resin and glass fibers are given in Table 1 (manufacturer data [26, 27]). The layup and geometrical description of the six plates are summarized in Table 2. Further details concerning the experimental program can be found in [7].

The crack propagation patterns obtained for one plate of each pair for the CFM, W50.50 and W60.40 plates are shown in Fig. 2. Results beyond the "last symmetric crack front" are not considered [7]. The experimental load vs displacement curves obtained are shown in Figs. 3, 4(a) and 5(a) for the CFM, W50.50 and W60.40 pairs of plates respectively. The load increased continuously up to specimen failure as a result of the non-proportional growth of the crack area [7]. Based on the compliance results (i.e. δ/P, where δ is the displacement and P is the load), two different regions were identified. Region A (indicated for the first plate of each pair) corresponds to the region where the experimental compliance decreased (i.e. stiffening of the system) and Region B to the region where it increased (i.e. softening of the region). The changing point in the compliance behavior ("transition point", TP) is indicated for all plates. The stiffening was caused by the stretching of the opening part of the plates as a result of the boundary conditions and the fiber-bridging generated in front of the crack tip. The softening was caused by the propagation of the crack itself. Both stiffening mechanisms were capable of delaying the softening of the system after crack initiation, i.e. Region A (stiffening) extended for all cases much further than the visual crack initiation, indicated also for all plates (denominated "Ini"), see Figs. 3-5. A more detailed discussion and further results can be found in [7].

4

2.2. Effects of stiffness variations on fiber-bridging development

Depending on the fiber architecture, the shape of the defect and the boundary conditions, 2D cracks may propagate following different patterns that can potentially lead to a non-homogeneous development of fiber-bridging along the crack front. As a result, the amount of total SERR required to propagate the crack can vary depending on the direction of propagation. Such behavior occurred in the W50.50 and W60.40 plates, whose woven fiber architecture caused the crack to propagate differently depending on the stiffness in the direction of propagation (see Fig. 2(b, c)) and thus the potential fiber-bridging to develop radially and circumferentially. To illustrate this behavior, an analysis of an arbitrary crack front following the propagation pattern of the W50.50 plates is presented in Fig. 6. As the crack propagated faster in the orthogonal directions (the stiffest with fibers at 0/90º) than along the diagonal directions (the least stiff with fibers at ±45º), an uneven deformation of the opened part of the plate occurred, exhibiting the largest opening along the orthogonal directions and the smallest along the diagonal directions (see Sections AA' in Fig. 6). This resulted in an additional circumferential opening and therefore to develop fiber-bridging both radially and circumferentially (circumferential Section BB'). The directions of propagation and fiber-bridging growth are indicated with arrows in Fig. 6. Due to the symmetric growth of the crack, only radial fiber-bridging developed along exactly the orthogonal and diagonal directions. However, the circumferential fiber-bridging was already present in close proximity to both directions. Consequently, the total SERR required to propagate the crack varied depending on the direction of propagation, being higher in those regions where more fiber-bridging developed. Similar behavior can be concluded for the W60.40 plates.

Only in particular cases, such as the in-plane isotropic CFM plates where the crack propagated similarly in all directions and therefore the fiber-bridging developed strictly radially (i.e. concentrically from the circular pre-crack, see Fig. 2(a)), is the required amount of total SERR the same all along the crack front.

3. Previous numerical results of CFM plates

A numerical investigation of the CFM plates was presented in [8] and the relevant results used to derive and validate the new method are summarized in the following. A three-dimensional finite element model was developed for the simulation of the experimental fracture response using cohesive elements. The traction-separation law used to model the behavior of the cohesive

elements, shown in Fig. 7(a), was a combination of two different laws: first, a linear softening law corresponding to the initial damage growth and second, an exponential softening law representing the fiber-bridging traction. The areas under the first and second parts equal the SERRs involved in crack initiation and fiber-bridging development respectively (G_{ini} and G_{br}). As discussed in [8], G_{ini} is a material property and G_{br} depends on the geometry and size of the investigated specimen. The addition of these two values corresponds to the total area under the traction-separation law (i.e. to the total SERR) and will be hereafter denoted as G_{tot} which therefore is also geometrical and size dependent. Further details regarding the numerical model and cohesive formulation can be found in [8].

The numerical load-displacement response obtained is shown in Fig. 3. Several relationships between the parameters of the traction-separation law and the load-displacement curves were observed [8]. The transition point (TP), which marked the full development of the FPZ, was reflected in the load-displacement curves as the change from an initially non-linear to a purely linear increasing behavior (see Fig. 3, Region B beyond the TP). It was further concluded that the slope of this linear part depended only on the value of the total SERR – i.e. greater slopes corresponded to greater total SERR values and vice versa – and was thus completely independent of the shape of the traction-separation law [8]. The method presented in this work was developed based on this last finding.

4. New total SERR derivation method

As mentioned in the introduction, existing fracture data reduction methods are not appropriate for determining the total SERR involved in 2D delamination. In order to overcome this problem, a numerically-based method to determine the total SERR involved in the Mode I-dominated 2D delamination of laminates with an embedded defect under opening loads was developed. The new method is based on the above-mentioned relationship between the total SERR (G_{tot}) and the slope of the load-displacement curves developed beyond the TP (hereafter referred to simply as "slope"). The method is described and applied for the in-plane isotropic CFM plates in the following and validated in Section 5 with the experimental results obtained for the orthotropic W50.50 and W60.40 plates.

Initially a three-dimensional (3D) FE model (of the CFM plate) with the elastic properties and geometry of the investigated plate and a zero-thickness layer of cohesive elements in the plane of the crack is developed (analogously to the one described in [8]). Considering that the slope

was found to be dependent of the area under the traction-separation law (i.e. G_{tot}) but independent of the shape of the traction-separation law, a simple traction-separation law with linear softening is used, in contrast to the model in [8], to define the cohesive behavior (see Fig. 7(b)) and implemented through a user material subroutine (UMAT) [8, 28]. The maximum traction for damage initiation is assumed to be 30% of the tensile strength of the matrix (84 MPa, [8, 27]), according to [8, 29], resulting in a value of $\sigma_c = 25.2$ MPa and the initial stiffness, K_0, is set to 100,000 MPa/mm [8, 28, 30]. Subsequently, five simulations with different values of G_{tot} (i.e. different areas under the traction-separation law and therefore different values of maximum opening), ranging from 2000 to 4000 J/m^2, are performed. The numerically obtained load-displacement curves are shown in Fig. 8. It can be observed that increasing slopes (denoted by "α") correspond to higher values of G_{tot} and higher loads. The α - G_{tot} values for each simulation are represented in Fig. 9, revealing a linear relationship between them; the equation of the fitted linear behavior is likewise indicated. Using the average value of the experimental slopes (0.280, see Fig. 3 and [7]), and entering the fitted equation, a value for G_{tot} of 3109 J/m^2 is obtained.

As discussed in Section 2.2, the total SERR (G_{tot}) required to propagate the crack may vary along the crack front depending on the fiber architecture, crack shape or boundary conditions. However, the load-displacement curve reflects the overall fracture behavior of the plates and therefore the slope (α) correlates with the overall or mean G_{tot} value required to propagate the 2D crack, hereafter denominated $\bar{G}_{tot}$:

$$\bar{G}_{tot} = \frac{\sum_{i=1}^{n} G_{tot,i} \cdot A_i}{A_{tot}} \tag{1}$$

where $G_{tot,i}$ is the total SERR required to locally propagate a crack area, A_i, along a particular direction and A_{tot} is the total propagated area (i.e. the summation of all A_i).

Similarly, and corresponding to the different G_{tot} values (ranging from a minimum to a maximum), different traction-separation laws may apply depending on the direction of propagation, see Fig. 10. However, in line with the mean value of G_{tot}, a mean traction-separation law, independent of the direction, can be, and is, assumed in the proposed method, thus simplifying the FE model significantly. In the case of the isotropic CFM plates, the same value of G_{tot} is required to propagate the crack in all directions (i.e. $G_{tot} = G_{tot,min} = G_{tot,max} = \bar{G}_{tot}$)

and therefore the mean traction-separation law coincides with the traction-separation law in every direction.

The new method can thus be broken down into the following six steps:

Step 1: development of an FE model comprising the geometry and elastic properties of the specimen with cohesive elements placed at the delamination interface.

Step 2: performance of FE analyses using the same simple linear-softening traction-separation law in all directions. Different values of $\bar{G}_{tot}$ are assigned to each analysis; at least three FE analyses with three different values of $\bar{G}_{tot}$ must be performed.

Step 3: extraction of the numerical load-displacement curves for each value of $\bar{G}_{tot}$ (i.e. for each analysis) and calculation of the corresponding values of the slope, α, of the last linear part of the curves.

Step 4: with the obtained α - $\bar{G}_{tot,}$ results, determination of the curve that provides the best fitting (a linear equation in the cases presented in this work).

Step 5: determination of the experimental slope of the linear part of the curves for each of the available specimens.

Step 6: using the fitted equation derived in Step 4 and with the average value of the experimental slopes obtained in Step 5, determination of the value of $\bar{G}_{tot}$.

The presented method does not require the crack front to be measured during the experiment in order to derive the total SERR, thereby avoiding any uncertainty linked to the location of the crack tip. The only experimental requirement is the load-displacement curve. Particularly in the case of 2D delamination of embedded cracks in opaque FRP materials such as carbon fiber-reinforced polymers (CFRPs), where measurement of the crack front is not visually possible, this represents a significant advantage. Furthermore, considering that the slope used in the method corresponds to a mean G_{tot} value, the procedure is valid for any fiber architecture, crack shape and boundary conditions. This $\bar{G}_{tot}$ value underestimates the G_{tot} in some regions and overestimates it in others, therefore resulting in an inaccurate propagation pattern. However, the aim of the method is not to determine the exact shape of the propagated crack, but to obtain a total SERR value that indicates whether a 2D crack propagates or not. In cases where an accurate prediction of the load-displacement behavior between crack initiation and the TP (see Figs. 3-5) and the crack propagation pattern is required, further modeling with varying traction-separation laws and optimized shape might be necessary, as shown in [8]. The value of the total

8

2D SERR provided by the presented method constitutes a valuable starting point for any further optimization of the traction-separation law.

5. Validation of the method and discussion

5.1. CFM laminates

The result of total SERR obtained by applying the described method for the CFM plates ($\bar{G}_{tot}$=3109 J/m^2) only differs by 3.5% from the numerically estimated value in [8] of 3000 J/m^2, where the complete load-displacement curve and the crack propagation pattern were accurately reproduced, representing therefore a first validation of the method.

5.2. W50.50 laminates

5.2.1. Validation

To further validate the method, the described procedure was applied to determine the value of the total SERR associated with the delamination experiments on the W50.50 plates described in Section 2.1 and [7]. According to Step 1, a 3D finite element model was developed using the commercial finite element analysis (FEA) software ABAQUS 6.14.1. The geometry and dimensions of the model are shown in Fig. 11. Only one quarter of the plate was modeled using the symmetry planes (D1 and D2) conforming to the experimentally recorded vertical movements of the free edges (see [7]). Symmetric boundary conditions were applied accordingly. The thickness of the laminate was selected as the average of the experimental thicknesses (i.e. 3.43 mm, see Table 2). As mentioned in Section 2.1, two steel inserts of 1.2-mm thickness and 100-mm diameter were used as part of the loading system [7], but, for the sake of simplicity, neither they nor the rest of the components of the loading system were explicitly modeled. Alternatively, all the nodes in the inner faces located inside the area delimited by the loading line ("reference area'' in Fig. 11) were tied with a rigid body condition [31] to reference points. The boundary conditions were applied to the reference points, i.e. in-plane displacements and all the rotations constrained in the top reference point and all displacements and rotations constrained in the bottom reference point. However, since the radius of this loading line is 35 mm and the radius of the steel inserts 50 mm, there was a remaining 15 mm of deforming plate (i.e. not included in the rigid body condition) with a modified section of both GFRP laminate and steel. Measuring the thickness of the laminate in this area, an average value of 0.8 mm was obtained which, added to the 1.2-mm thickness of the steel inserts, resulted in a section of 2-mm thickness. The properties of this modified section were calculated by applying the Composite Laminate Theory (CLT) for the in-plane properties

and the Rule of Mixtures (ROM) for the out-of-plane properties. The engineering constants used for the laminate (W50.50) and modified section (W50.50+steel) are presented in Table 3.

A single zero-thickness layer of three-dimensional built-in cohesive elements of eight nodes (Abaqus/Standard COH3D8, [31]) was implemented at the midplane of the un-cracked region (i.e. the delamination interface, see Fig. 11). The bulk material (GFRP) was meshed using built-in continuum shell elements of eight nodes and reduced integration (Abaqus/Standard CS8R, [31]). Two through-thickness elements were assigned to each of the halves of the plate (i.e. above and below the delamination interface), this being sufficient to accurately capture the bending behavior (see [8]). A finer mesh was assigned around the end of the pre-crack (indicated as a_0 in Fig. 11) and at the previously described section-transition zone (from modified steel/GFRP to pure GFRP section). The largest dimension of the elements was 0.981 mm at the end of the pre-crack and 0.552 mm in the section-transition zone. Close to the free edges, elements with a maximum dimension of 3.258 mm were used. The model comprised 387,440 nodes and 299,988 elements.

To determine whether, apart from the dominant opening mode (Mode I)), shear fracture modes (Mode II and Mode III) were contributing to the propagation of the crack, shear displacements in the cohesive elements were also computed. Insignificant values were obtained throughout the simulation, confirming a pure opening mode at the crack tip.

In Step 2, four FE analyses were performed considering four different values of $\bar{G}_{tot}$ (600, 1000, 1250 and 1500 J/m^2). The traction-separation laws used corresponding to the indicated values of $\bar{G}_{tot}$, are also presented in Fig. 7(b) (again implemented through a UMAT). Subsequently, and according to Step 3, the numerical load-displacement curves were extracted (see Fig. 12), and the slopes (α) corresponding to each value of $\bar{G}_{tot}$ were derived; the α - $\bar{G}_{tot}$ pairs obtained are plotted in Fig. 13. A linear relationship was also obtained and the equation of the fitted line is likewise indicated.

Due to the nature of the woven reinforcement, a typical "run-arrest" behavior [32] in the experimental load-displacement curves was obtained (see Fig. 4(a)). Therefore, to determine the experimental slopes (Step 4), only the segments between the small jumps were considered (see Fig. 4(b)), i.e. 4 to 5 segments were selected in a way to minimize their standard deviation. Each of the computed segments is indicated in red with ordinal numbers. An average slope was

obtained for each of the plates. Finally, and following Steps 5 and 6, the mean value of both experimental slopes (i.e. 0.159) was entered in the fitted equation in Fig. 13. A value of $\bar{G}_{tot}$=1297 J/m^2 was obtained. A new simulation using this value and also a simple linear-softening traction-separation law was then performed. The resulting load-displacement curve is shown in Fig. 12. A fairly good agreement with the experimental results, beyond the TP, was obtained. The slopes compared well while the average load level of the two experiments was only slightly overestimated (approximately a 10%); the latter was attributed to the experimental scatter exhibited for this type of plate, which was higher than in the CFM (Fig. 3) and W60.40 (Fig. 5) plates.

5.2.2. *Comparison with DCB fracture results and discussion*

For comparison between the 2D total SERR obtained in the previous section and the 1D total SERR corresponding to the same fiber architecture, DCB specimens were fabricated and investigated. In order to examine whether the stiffness (different depending on the orientation of the woven fabrics) had any effect on the 1D fracture behavior, one specimen with the layers of woven fabric oriented at 0/90º and another at ±45º degrees (both with respect to the longitudinal direction of the DCB specimen) were investigated, as indicated in Fig. 2(b). The specimens were 25 mm wide and 6.55 mm thick. They were cut from a new laminate fabricated with the same lay-up as that used in the W50.50 plates (i.e. eight layers of reinforcement - see Table 2) using the vacuum infusion technique. A Teflon film of 13µm thickness was placed at the midplane to introduce the pre-crack. Similar infusion and curing protocols to those of the plates were used [7]. The load was transferred from the loading frame to the specimens with patented mechanically fixed loading blocks [33]. The experiments were performed under displacement-control on a 5-kN MTS Insight electromechanical machine with a load cell calibrated from 1 to 100% of its maximum capacity at a displacement rate of 5 mm/min. All the experiments were conducted under laboratory conditions, 23±2ºC and 50±5% RH and according to the ISO 15024 standard [2]. The crack length was monitored from one side of the specimen where a thin coat of white paint was applied. A video acquisition system comprising a Canon 550D digital camera installed on a travelling fixture was employed to optically monitor the crack. Vertical markers were drawn each millimeter between a 1- and 5-mm distance from the crack tip and each 5 millimeters from a 5- to 50-mm distance.

The experimental load vs displacement curves for the two configurations of DCB (0/90º and ±45º) are presented in Fig. 14(a). They exhibited the so-called "run-arrest" behavior [32] in the

descending branch due to the unstable crack propagation typical of woven fabric composites. The total strain energy release rate (G_{tot}) was calculated using the experimental compliance method (ECM) [34] and the derived R-curves are shown in Fig. 14(b). It can be observed that similar values were obtained for both specimens, leading to the conclusion that there were no relevant differences in the 1D fracture behavior as a result of the orientation of the fabric. A limited amount of fiber-bridging was observed (Fig. 14(b), with an increase of G_{tot} from approx. 800 to 1000 J/m^2), which is typical in woven fabric DCB specimens [32].

Similarly to what was observed in the CFM plates (see [8]), where the total SERR increased by 50% in comparison to the DCB specimens due to an increase in the fiber-bridging, the total SERR value obtained for the W50.50 plates was approximately 30% higher than the total SERR derived from the DCB specimens (~1300 vs ~1000 J/m^2). This increase was likewise assumed to also be caused by an increase in the fiber-bridging. This is further confirmation of the influence of the stiffness-related effects (see [8]) in 2D delamination cases.

As discussed in Section 2.2, additional transversal fiber-bridging developed in the case of the W50.50 plates as a result of the uneven opening of the deformed part of the plate. To confirm this, the out-of-plane displacement profile along a circumferential path at an 85-mm distance from the center of the plate (i.e. 5 mm before the end of the pre-crack), extracted from the last FE model (i.e. with a $\bar{G}_{tot}$=1297 J/m^2) at an opening displacement of ~26 mm, is presented in Fig. 15. It can be observed that along the stiffest direction (i.e. the orthogonal 0/90º direction) the out-of-plane displacement was significantly higher than along the diagonal directions (±45º), causing the transversal crack growth and corresponding fiber-bridging. Therefore, the transversal fiber-bridging constitutes a further 2D effect, which can also be likewise amplified by the stiffness-related effects. In cases where no fiber-bridging develops, none of the described 2D effects would apply.

5.3. W60.40 laminates

A last validation of the method was carried out using the experimental results of the W60.40 plates. The 3D FE model (Step 1) was developed also using the commercial FEA software ABAQUS 6.14.1 and its geometry and dimensions are shown in Fig. 16. Half of the plate was modeled using the symmetry plane "A" according to the experimental behavior of the free edges (see [7]) and a symmetry boundary condition was correspondingly applied. The thickness of the laminate was the average of the experimental thicknesses, i.e. 3.055 mm (Table 2). As in

the FE model of the W50.50 plates, the loading system was not explicitly modeled and all the nodes in the inner faces inside the loading line were tied using a rigid body condition [31] to reference points (Fig. 16). The boundary conditions (same as for the W50.50 model) were applied to the reference points. The same method as that described in Section 5.1 to characterize the modified section of steel and GFRP was followed. The engineering constants used to define the pure bulk material (GFRP) and the composite section are presented in Table 3. The same type of elements as in the W50.50 FE model were used in both bulk and cohesive sections (see Section 5.1). The largest dimension of the elements close to the end of the pre-crack was 0.896 mm. Also a finer mesh was used at the transition from the modified GFRP/steel section to pure GFRP section, with elements whose largest dimension was 0.495 mm. Elements of 2.562 mm (also the largest dimension) were used close to the boundaries. The model comprised 642,806 nodes and 490,880 elements and insignificant values of cohesive shear displacement were also obtained throughout the simulation, again confirming a pure opening fracture mode. No contribution of shear fracture modes was found.

Four different values of $\bar{G}_{tot}$ (600, 1200, 1600 and 2000 J/m^2) were used to evaluate the α - $\bar{G}_{tot}$ behavior (one simulation for each value, Step 2). The traction-separation laws used (also the same in all directions as for the W50.50 plates) are shown in Fig. 7(b) and the numerical load-displacement curves obtained for each simulation are presented in Fig. 17 (Step 3). The extracted α - $\bar{G}_{tot}$ pairs are represented in Fig. 18 together with the equation also fitting a linear behavior (Step 4). Again, due to the woven nature of the reinforcement, a "run-arrest" behavior occurred and the experimental slopes (Step 5) were thus again determined by considering only the segments between the irregularities (see Fig. 5(b)) following the same procedure as in Section 5.1.1. The mean value of both experimental slopes was 0.120, which, according to the fitted equation in Fig. 18, provided a value of $\bar{G}_{tot}$ =1382 J/m^2 (Step 6). As for the W50.50 plates, a new simulation using this value and also a simple linear-softening traction-separation law was performed. The load-displacement curve obtained is shown in Fig. 17. Good agreement with the experimental results for the slope and load level of the linear part of the curves was obtained.

6. Conclusions

A numerically-based method to determine the total SERR involved in the Mode I-dominated 2D delamination of GFRP laminates with internal embedded defects and subjected to opening loads was presented in this work. The method is based on the relationship between the slope of

the load-displacement curves after the full development of the FPZ and the total SERR involved in the delamination process. The equation relating both parameters (linear for the studied cases) is derived from three-dimensional FE analysis using simple linear-softening cohesive zone models. The above-mentioned slope and total SERR correspond to the overall 2D fracture behavior. Thus, the same mean linear-softening traction-separation law is implemented in every direction, simplifying considerably the computational effort. The total 2D SERR is obtained by substituting the corresponding slope of the load-displacement experimental curves in the derived equation. Even though with this method the total SERR value along certain directions may be locally overestimated or underestimated, therefore resulting in an inaccurate crack propagation pattern, it can however assure that no unstable propagation of the crack area occurs. The method is thus suitable for damage-tolerant designs. The crack front does not need to be monitored throughout the experiment since the load-displacement curves are the only experimental input required. This constitutes a considerable simplification in the experimental process, reducing time and instrumentation, particularly in opaque laminates offering no visual access to the crack.

The method was validated using the experimental results obtained for three types of GFRP/epoxy plates with different fiber architectures. Further validation with different materials is however still recommended. The presented method is valid for any fiber architecture, crack shape and boundary conditions in Mode I-dominated and opening loading cases. If shear fracture mode contributions would arise, the presented method would not be applicable.

The total SERR obtained by applying the method for one of the validation plates (W50.50) was compared to the total SERR obtained from DCB specimens composed of the same material. The total SERR obtained for the plates was 30% greater than for the DCBs. As for the CFM plates, this was caused by an increment in the amount of fiber-bridging, which in this case developed both radially and circumferentially, as a result of the increase in the bending stiffness (from beam to plate), its uneven distribution and the stress-stiffening effect. This constitutes further confirmation of the relevant role of stiffness effects on the development of fracture mechanisms in 2D delamination.

Data availability statement

The data required to reproduce these findings cannot be shared at this time as the data also forms part of an ongoing study.

References

1. Benzeggagh, M.L., Kenane, M. Measurement of mixed-mode delamination fracture toughness of unidirectional glass/epoxy composites with mixed-mode bending apparatus. Compos. Sci. Technol., 1996; 56: 439–449.

2. ISO 15024:2001: Fibre-reinforced plastic composites — Determination of the mode I interlaminar fracture toughness, GIC, for unidirectionally reinforced materials (83.120 – Reinforced Plastics).

3. ISO 15114:2014: Fibre-reinforced plastic composites — Determination of the mode II fracture resistance for unidirectionally reinforced materials using the calibrated end-loaded split (C-ELS) test and an effective crack length approach (83.120 – Reinforced Plastics).

4. ASTM D6671/D6671M - 13e1: Standard test method for mixed mode I-mode II interlaminar fracture toughness for unidirectional fiber-reinforced polymer matrix composites, in Annual book of ATM standards: adhesive section 15.03.

5. Chen, Z.M., Krueger, R., Rinker, M. Facesheet/Core Disbond Growth in Honeycomb Sandwich Panels Subjected to Ground-Air-Ground Pressurization and In-Plane Loading. In: 11th International Conference on Sandwich Structures ICSS-11, Ft. Lauderdale, USA, March, 2016.

6. Riccio A., Gigliotti M. A novel numerical delamination growth initiation approach for the preliminary design of damage tolerant composite structures. J. Comp. Mat., 2007;41(16):1939:1960.

7. Cameselle-Molares A., Vassilopoulos A.P., Keller T. Experimental investigation of two-dimensional delamination in GFRP laminates. Eng. Frac. Mechs., 2018; 203: 152-171.

8. Cameselle-Molares A., Vassilopoulos A.P., Renart J., Turon A., Keller T. Numerical simulation of two-dimensional in-plane crack propagation in FRP laminates. Comp. Struc. 2018; 200: 396-407.

9. Shaverdi M., Vassilopoulos A.P., Keller T. Modelling effects of asymmetry and fiber bridging on Mode I fracture behavior of bonded pultruded composite joints. Eng. Fract. Mech., 2013; 99; 335-348.

10. Cameselle-Molares A., Roohollah S., Shaverdi M., Vassilopoulos A.P., Keller T. Fracture mechanics-based progressive damage modelling of adhesively bonded fibre-reinforced polymer joints. Fatigue Fract. Eng. Mater. Struct., 2017; 40(12): 2183-2193.

11. Pappas G, Canal L.P., Botsis J. Characterization of intralaminar mode I fracture of AS4/PPS composites using inverse identification and micromechanics. Composites: Part A, 2016; 91; 117-126.

12. Suo Z., Bao G., Fan B. Delamination R-curve phenomena due to damage. J. Mech. Phys. Solids, 1992; 40 (1): 1-16.

13. Manshadi B.D., Vassilopoulos A.P., Botsis J. A combined experimental/numerical study of the scaling effects on mode I delamination of GFRP. Comp. Science and Tech., 2013; 83; 32-39.

14. Canal L.P., Alfano M., Botsis J. A multi-scale based cohesive zone model for the analysis of thickness scaling effect in fiber bridging. Comp. Science and Tech., 2017; 139; 90-98.

15. Bao G., Suo Z. Remarks on crack-bridging concepts. Appl. Mech. Rev., 1992; 45(8); 355-366.

16. Farmand-Ashtiani E., Cugnoni J., Botsis J. Specimen thickness dependence of large scale fiber bridging in mode I interlaminar fracture of carbon epoxy composite. Inter. J. of Solids and Struct., 2015; 55; 58-65.

17. Blackman B.R.K., Kinloch A.J., Paraschi M. The determination of the mode II adhesive fracture resistance, G_{IIc}, of structural adhesive joints: an effective crack length approach. Eng. Fract. Mechs., 2005; 72: 877-897.

18. Rice J. A path independent integral and the approximate analysis of stain concentration by notches and cracks. J. Appl. Mech., 1968; 35:379-386.

19. Pérez-Galmés M., Renart J., Sarrado C., Rodríguez-Bellido A., Costa J. A data reduction method based on the J-integral to obtain the interlaminar fracture toughness in a mode II end-loaded split (ELS) test. Composites: Part A, 2016;90:670-677.

20. Que N.S., Tin-Loi F. An optimization approach for indirect identification of cohesive crack properties. Comput. Struct., 2002; 80: 1383-92.

21. Xu, Y., Li, X., Wang, X., Liang, L. Inverse parameter identification of cohesive zone model for simulating mixed-mode crack propagation. Int. J. Solids and Struct., 2014; 51: 2400-2410.

22. Dourado N., de Moura M.F.S.F., de Morais A.B., Pereira A.B. Bilinear approximations to the mode II delamination cohesive law using an inverse method.

23. De Moura M.F.S.F., Morais J.J.L., Dourado N. A new data reduction scheme for mode I wood fracture characterization using the double cantilever beam test. Eng. Frac. Mechs., 2008; 75: 3852-65.

24. Valoroso, N., Sessa, S., Lepore, M., Cricri, G. Identification of mode-I cohesive parameters for bonded interfaces based on DCB test. Eng. Frac. Mechs., 2013; 104: 56-79.

25. Ortega A., Maimí P., González E.V., Trias D. Characterization of the translaminar fracture cohesive law. Composites: Part A, 2016; 91: 501-509.

26. Owen's Corning Reinforcements Composite Solutions Guide. <http://www.ocvreinforcements.com/pdf/library/Composite_Solutions_Guide_100360_E_finalprintable.pdf> (Accessed 26 March 2018).

27. Sika datasheet product. <https://deu.sika.com/dms/getdocument.get/dd4b783e-bfa5-32e3-a705-f9f548f6b326/Biresin_CR83_eng.pdf> (Accessed 19 October 2017).

28. Turon A., Camanho P.P., Costa J., Dávila C.G. A damage model for the simulation of delamination in advanced composites under variable-mode loading. Mechanics of Materials, 2006; 38(11): 1072–1089.

29. Camanho P.P., Dávila C.G., Ambur D.R. Numerical simulation of delamination growth in composite materials. NASA/TP-2001-211041. Hampton: NASA Langley Research Center; 2001.

30. Turon A., Camanho P.P., Costa J., Renart J. Accurate simulation of delamination growth under mixed-mode loading using cohesive elements: Definition of interlaminar strengths and elastic stiffness. Composite Structures, 2010; 92(8): 1857–1864.

31. Abaqus Inc. Abaqus analysis user's manual, version 6.14-1. 2014. Providence, RI, USA.

32. Blake S.P., Berube K.A., Lopez-Anido R.A. Interlaminar fracture toughness of woven E-glass fabric composites. J. Comp. Mat., 2011; 46(13): 1583:1592.

33. Renart J., Blanco N., Pajares E., Costa J., Lazcano S., Santacruz G. Side Clamped Beam (SCB) hinge system for delamination tests in beam-type composite specimens. Comp. Sc. and Tech., 2011; 71; 1023-1029.

34. Anderson Ted. Fracture mechanics. 2nd ed. Texas: CRP; 1995.

Tables:

Table 1. Material properties

Material	E (GPa)	G (GPa)	ν (-)	ρ (g/cm³)
Epoxy resin	2.96	1.30	0.35	1.14
E-CR* glass (for CFM)	80.00	32.80	0.22	2.62
E-glass (for woven)	72.00	29.50	0.22	2.55

*CR: Corrosion Resistant

Table 2. Description of GFRP laminated plates

Plate type	No. of layers	Reinforcement weight per layer (g/m²)	Dimensions (mm) (width x height x avg. thickness)
CFM.1/CFM.2	6	600	420x420x7.50/420x420x6.99
W50.50.1/W50.50.2	8	390	460x460x3.33/480x480x3.53
W60.40.1/W60.40.2	6	500	410x410x3.05/410x410x3.06

Table 3. Elastic properties of laminated plates used in FE models

Plate type	E_1 (GPa)	E_2 (GPa)	E_3 (GPa)	G_{12} (GPa)	G_{13} (GPa)	G_{23} (GPa)	ν_{12} (-)	ν_{13} (-)	ν_{23} (-)
W50.50	17.79	17.79	7.25	2.62	1.83	1.83	0.19	0.33	0.33
W50.50 + steel	89.51	89.51	46.82	30.42	6.43	6.43	0.25	0.30	0.30
W60.40	22.30	14.86	7.57	1.76	2.00	1.73	0.23	0.32	0.33
W60.40 + steel	131.99	111.69	116.63	33.57	11.74	7.48	0.29	0.29	0.30

Figures:
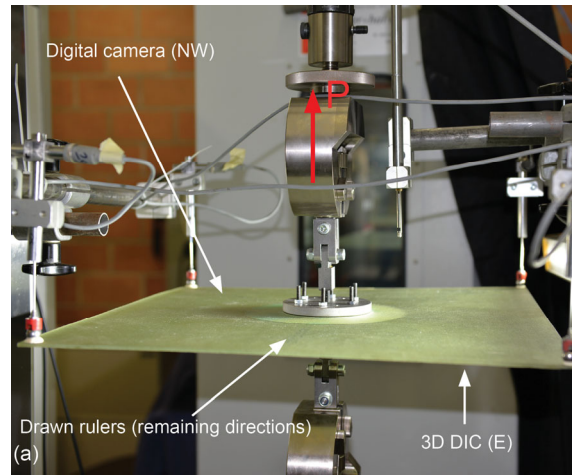
Fig. 1. Experimental set-up and crack measuring system
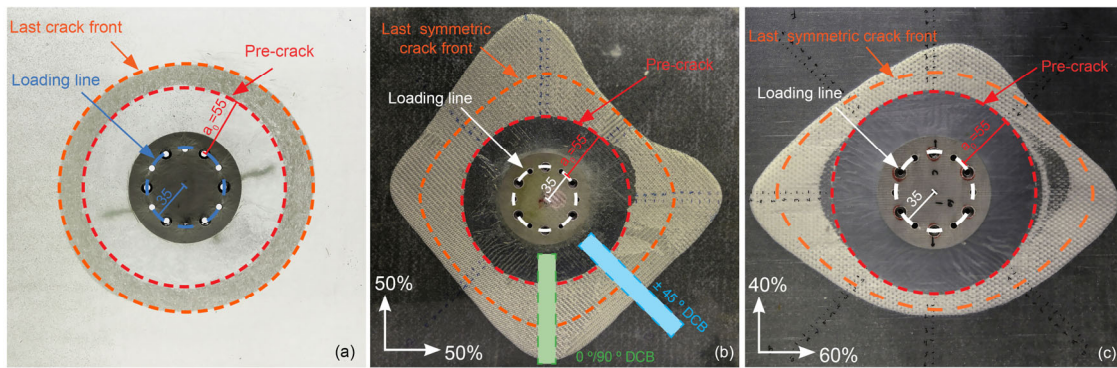
Fig. 2. Crack propagation patterns in plates (a) CFM.1; (b) W50.50.1 and (c) W60.40.2; dimensions in mm
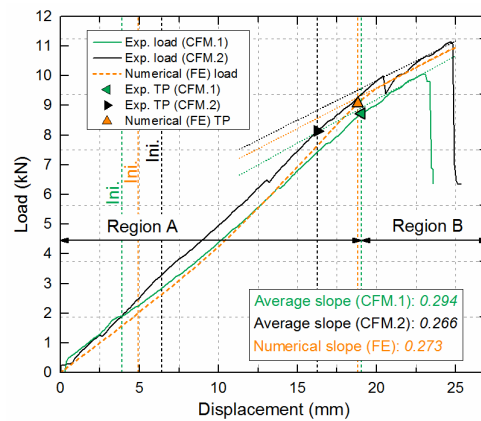
Fig. 3. Experimental and numerical load vs opening displacement curves of CFM plates and slopes in Region B
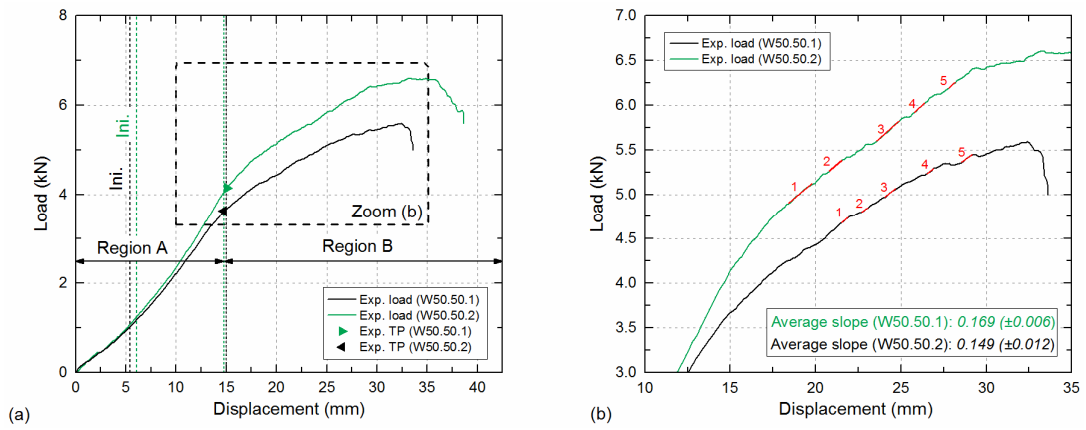
Fig. 4. (a) Experimental load vs opening displacement curves of W50.50 plates; (b) extraction of experimental slopes
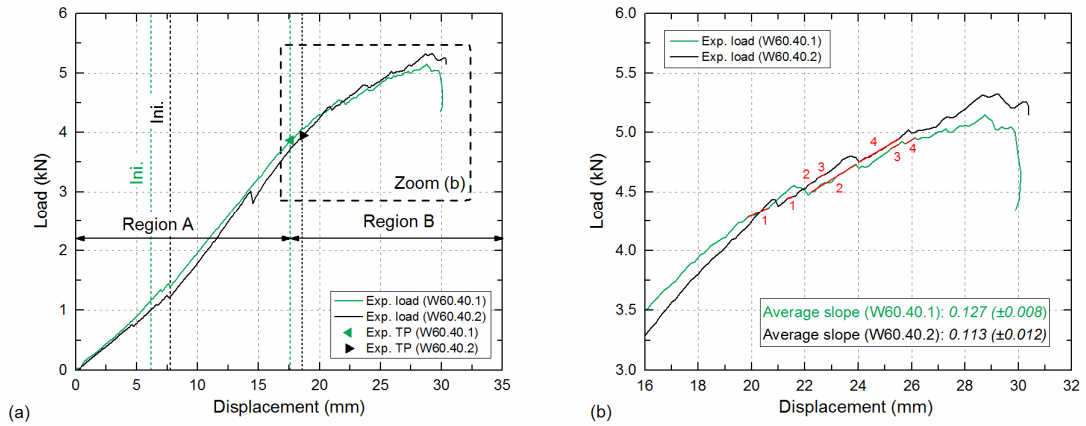
Fig. 5. (a) Experimental load vs opening displacement curves of W60.40 plates; (b) extraction of experimental slopes
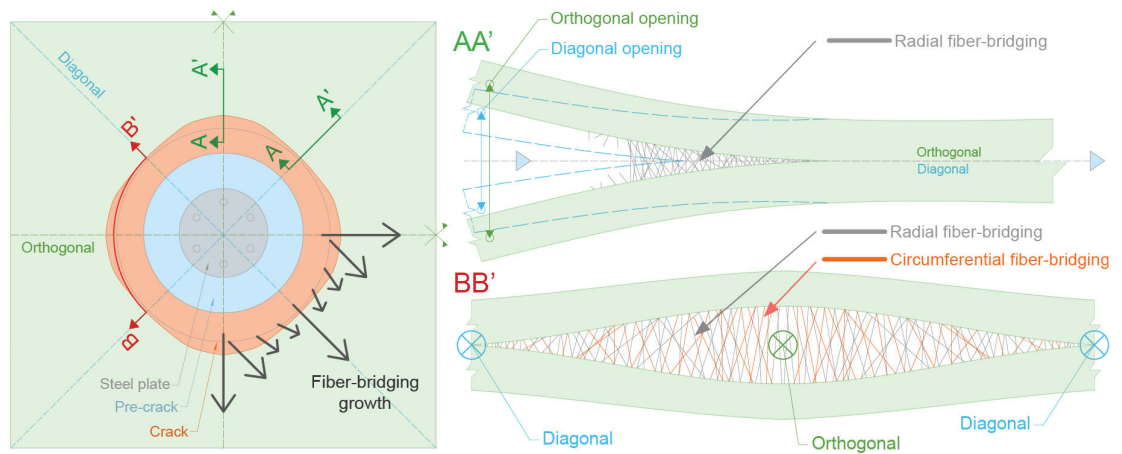
Fig. 6. Explanatory layout of radial and circumferential fiber-bridging development (not to scale)
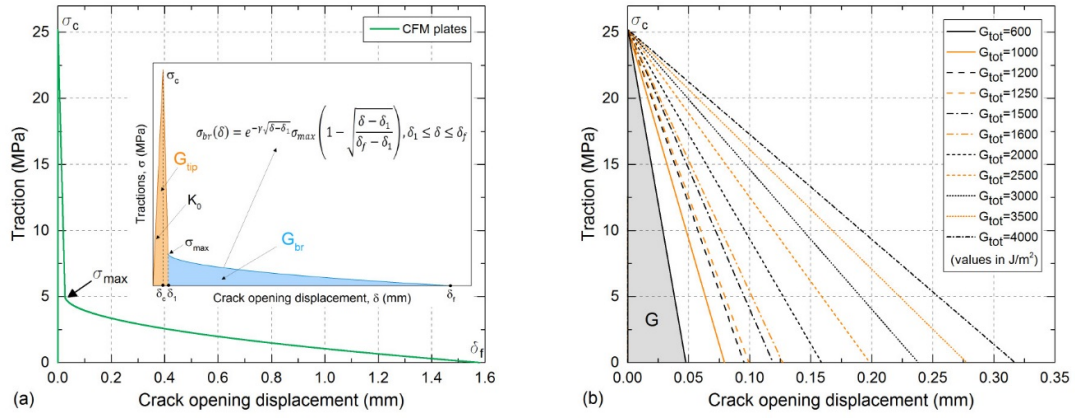
Fig. 7. Traction-separation curves used in numerical models; (a) with softening including bridging law used for CFM; (b) with linear softening, used for total SERR derivation in proposed method (G_{tot} for CFM and $\overline{G}_{tot}$ for woven plates)
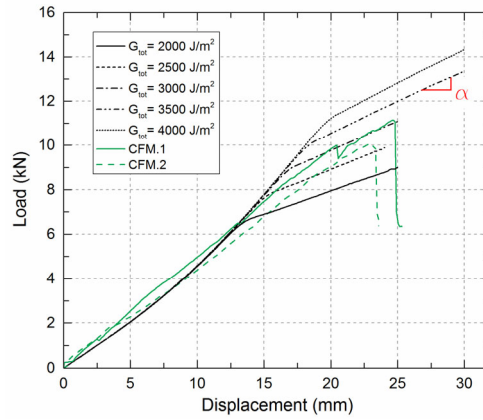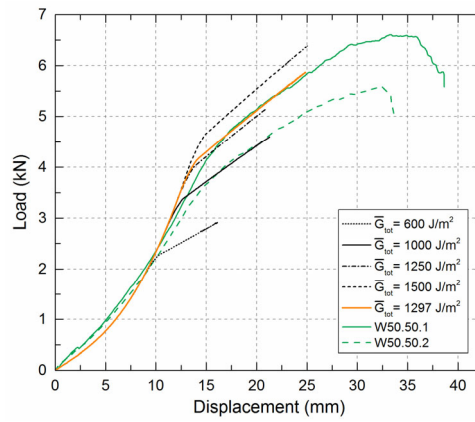

Fig. 8. Numerical load vs opening displacement curves obtained for CFM laminates using different values of G_{tot} and a linear-softening cohesive law (see Fig. 7(b)) compared to experimental curves
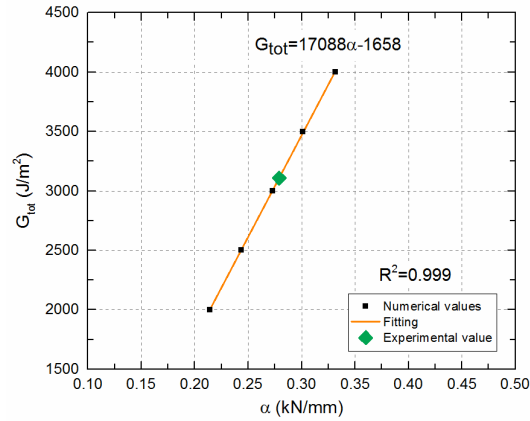
Fig. 9. Numerical α vs G_{tot} curve obtained for CFM laminates
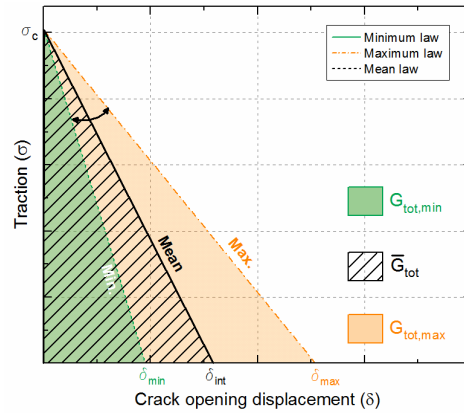
Fig. 10. General description of linear traction-separation laws varying along crack front
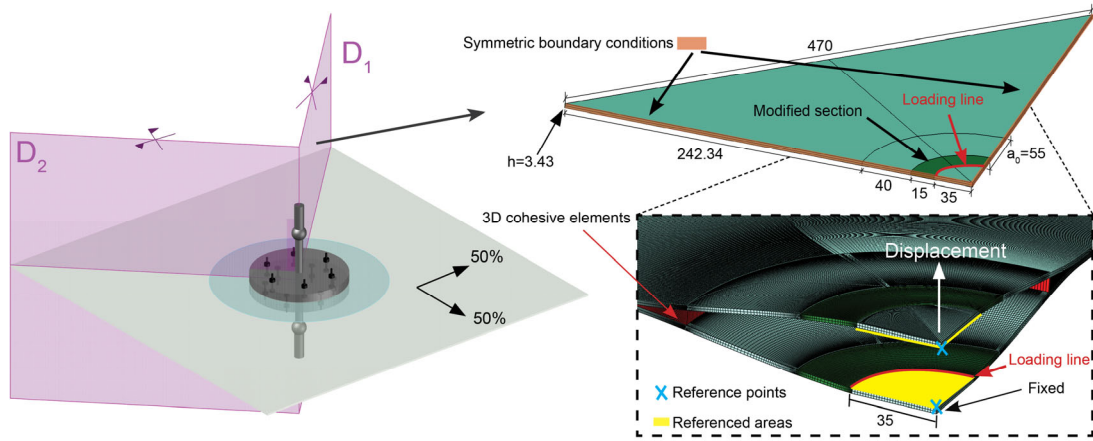
Fig. 11. Description of finite element model of W50.50 laminated plate. Dimensions in mm

Fig. 12. Numerical load vs opening displacement curves obtained for W50.50 laminates using different values of $\bar{G}_{tot}$ and a linear-softening cohesive law (see Fig. 7(b)) compared to experimental curves
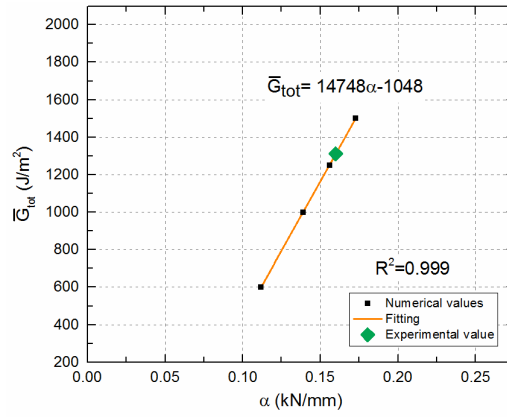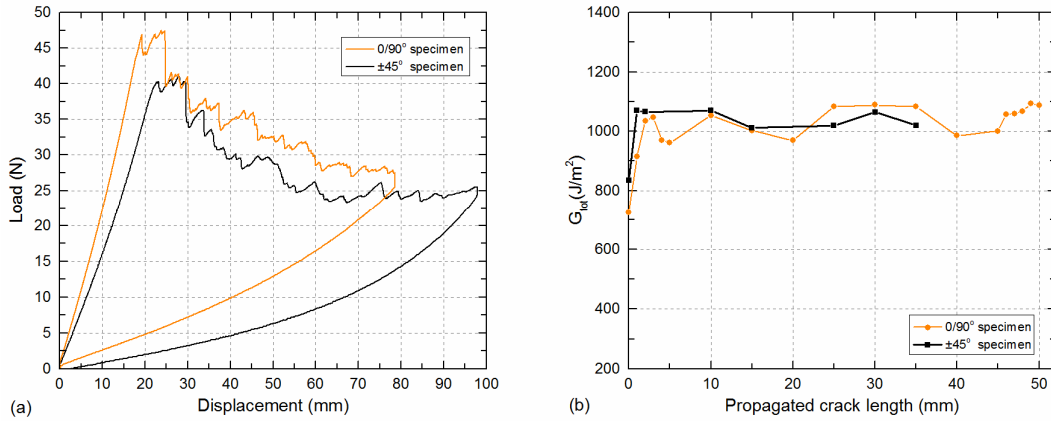
Fig. 13. Numerical α vs $\overline{G}_{tot}$ curve obtained for W50.50 laminates

Fig. 14. (a) Experimental load-displacement curves and (b) R-curves of W50.50 DCB specimens
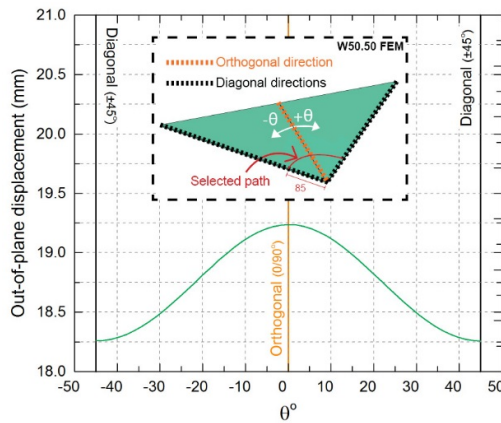
Fig. 15. Example of out-of-plane displacement profile at cracked region in W50.50 plates. Dimensions in mm
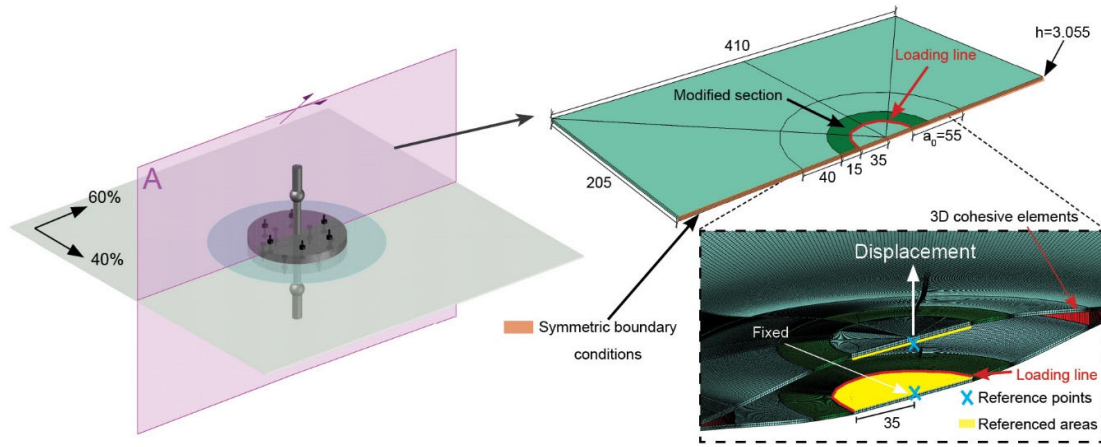
Fig. 16. Description of finite element model of W60.40 laminated plate. Dimensions in mm
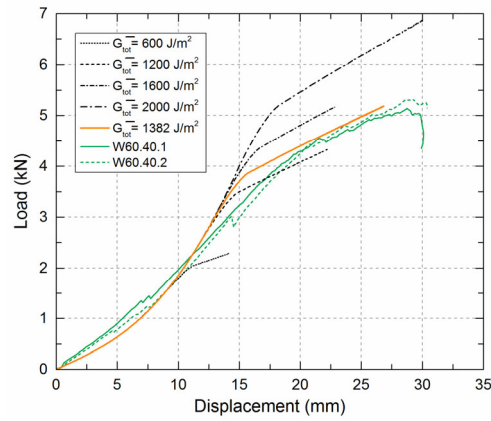

Fig. 17. Numerical load vs opening displacement curves obtained for W60.40 laminates using different values of $\bar{G}_{tot}$ and a linear-softening cohesive law (see Fig. 7(b)) compared to experimental curves
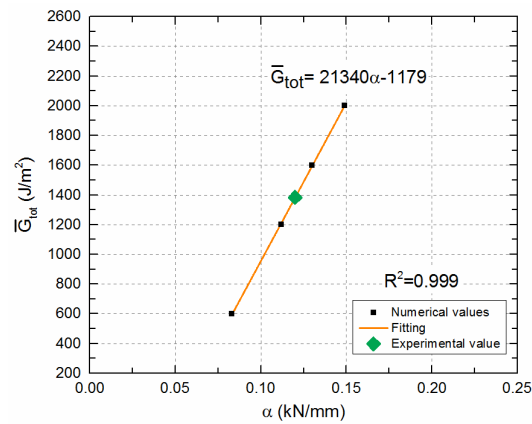

Fig. 18. Numerical α vs $\bar{G}_{tot}$ curve obtained for W60.40 laminates